The Impact of Meanders, Deepening and Broadening, and Seasonality on Agulhas Current Temperature Variability

K. McMonigal,[a] Lisa M. Beal,[a] Shane Elipot,[a] Kathryn L. Gunn,[a] Juliet Hermes,[b] Tamaryn Morris,[c] and Adam Houk[a]

[a] *Rosenstiel School of Marine and Atmospheric Sciences, University of Miami, Miami, Florida;* [b] *Egagasini Node, South African Environmental Observation Network, Cape Town, South Africa;* [c] *South African Weather Service, Cape Town, South Africa*

(Manuscript received 27 January 2020, in final form 28 August 2020)

ABSTRACT: For the first time, the temperature transport of the Agulhas Current is quantified in a time series. Over a 25-month mooring deployment at 34°S, seven tall moorings were instrumented to measure current velocity, temperature, and salinity. Current- and pressure-recording inverted echosounders were used to extend geostrophic velocity, temperature, and salinity records to 300 km offshore. In the mean, the current transports 3.8 PW of heat southward relative to 0°C: −76 Sv ($1\ \text{Sv} \equiv 10^6\ \text{m}^3\ \text{s}^{-1}$) at a transport-weighted temperature of 12.3°C. A 0.9-PW standard deviation in temperature transport is due to variability in both volume transport and the temperature field. Meandering of the current core dominates variability in the temperature field by warming temperatures offshore and cooling temperatures near the coast. However, meandering has a limited impact on the temperature transport, which varies more closely with a deepening and broadening of the current associated with an inshore isotherm shoaling and an offshore isotherm deepening. Stronger southward temperature transports correspond to a deeper current transporting more volume, yet at a cooler transport-weighted temperature. Seasonality is not observed in the temperature transport time series, possibly because of the offsetting effects of cooler temperatures during times of seasonally stronger volume transports. Although volume transport and temperature transport are highly correlated, the large variability in transport-weighted temperature means that using volume transport alone to infer temperature transport results in an error that could be as large as 24% of the southern Indian Ocean heat transport.

KEYWORDS: Indian Ocean; Boundary currents; Mass fluxes/transport; Boundary currents; Mass fluxes/transport

1. Introduction

The Agulhas Current is the western boundary current of the southern Indian Ocean subtropical gyre. It is a warm, strong, poleward-flowing current. As such, it transports large amounts of water and heat. The temperature of the current has impacts on local weather and climate, including extreme events and rainfall (Mohino et al. 2011; Rouault 2002; Njouodo et al. 2018). The current also plays a dominant role in the basin wide Indian Ocean heat budget (Bryden and Beal 2001). Therefore, it is important to understand the structure and variability of the Agulhas Current temperature and temperature transport.

A 3-yr time series of the volume transport of the Agulhas Current was previously constructed using data from the 2010–13 Agulhas Current Time-series (ACT) experiment (Beal et al. 2015). Additionally, a volume transport proxy was created to extend the time series to the full satellite record (Beal and Elipot 2016). These studies revealed that the time-averaged volume transport of the current is -77 ± 5 Sv ($1\ \text{Sv} \equiv 10^6\ \text{m}^3\ \text{s}^{-1}$) using a boundary layer definition and -84 ± 11 Sv using a stream-wise definition, with standard deviations of 32 and 24 Sv, respectively (Beal et al. 2015). The current is highly variable on time scales from days to interannual. A 20-Sv peak-to-peak seasonal cycle was found, with largest southward volume transports in austral summer, and smallest in austral winter (Beal et al. 2015). The phasing of the seasonality can be explained by baroclinic adjustment to the seasonal cycle in near field winds (Hutchinson et al. 2018). Variability in Agulhas Current volume transport has also been linked to El Niño–Southern Oscillation and the southern annular mode (Elipot and Beal 2018).

The Agulhas Current has not strengthened over the satellite record and has instead broadened as a result of increased meandering (Beal and Elipot 2016). During a meander, the core of the current moves offshore by 50–200 km (Leber and Beal 2014; Elipot and Beal 2015), due at least in part to barotropic instability (Elipot and Beal 2015; Tsugawa and Hasumi 2010). Upwelling leads to a decrease in temperature of up to 9°C over the continental shelf (Leber et al. 2017; Goschen et al. 2015). The streamwise volume transport of the current remains largely unchanged during meanders, as the decrease in peak current speeds is offset by a broadening and deepening of the current (Leber and Beal 2014). A mean of 1.6 meanders occurred per year between 1993 and 2013, with meanders linked to the shedding of some Agulhas rings (Elipot and Beal 2015; Rouault and Penven 2011).

Although the velocity and volume transport variability of the Agulhas Current have been well characterized, observations of the subsurface temperature have previously been limited to hydrographic crossings at discrete points in time. These observations do not fully cover the seasonal cycle, and

Denotes content that is immediately available upon publication as open access.

Supplemental information related to this paper is available at the Journals Online website: https://doi.org/10.1175/JPO-D-20-0018.s1.

Corresponding author: K. McMonigal, kmcmonigal@rsmas.miami.edu

Publisher's Note: This article was revised on 4 March 2022 to make available a corrected version of the associated supplemental file, as explained corrigendum to this article.

DOI: 10.1175/JPO-D-20-0018.1

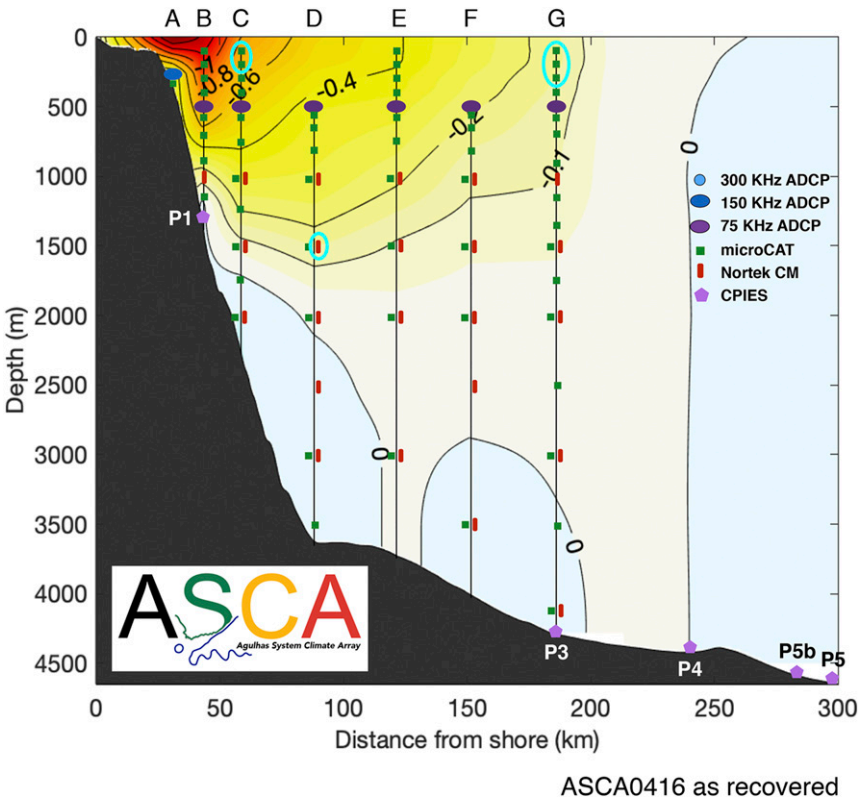

FIG. 1. The ASCA as recovered in June 2018. The background colors show the 2-yr mean current velocity as measured by the ASCA. Data were recovered from all instruments except those circled in cyan.

can alias unsteady processes, such as meandering. The Argo array provides many temperature and salinity profiles within the current, however, it does not capture flow in depths of less than 2000 m and cannot resolve the cross-sectional temperature structure of the current. Here, we present the first time series of the subsurface temperature structure of the Agulhas Current. We investigate the temperature cross section and temperature transport of the current over the April 2016–June 2018 deployment of the Agulhas System Climate Array (ASCA). ASCA was a collaboration between South African, Dutch, and U.S. scientists to measure the time-varying temperature and salinity transports of the Agulhas Current for the first time. The array design followed that of ACT (Beal et al. 2015), with the addition of measurements of thermohaline properties by microCATs deployed on Dyneema (manufactured by DSM N.V.) tails above the acoustic Doppler current profilers (ADCPs), and throughout the water column below (Fig. 1). We find that the temperature field and temperature transport are linked to three distinct modes of variability: the meandering mode, a deepening and broadening mode, and a surface-limited seasonal mode.

2. Data and methods

a. Velocity data: Current meters and ADCPs

Seven ACDPs and 25 current meters recorded hourly current velocity and instrument pressure. One ADCP and seven current meters did not record data for the full deployment time period (Fig. 2). Before interpolating the velocity data to a regular grid, we first extend these shorter records by applying sequential multiple regression models based on nearby instrumental records, such as those above or below on the same mooring, or at a similar depth on an adjacent mooring (arrows in Fig. 2a).

After extending all instrument records to full length, the velocity records are 40-h low-pass filtered and subsampled to 20-h time steps. Then, the data are interpolated to a regularly spaced, 500-m horizontal, 20-dbar vertical grid using the same method as for the Agulhas Current Time-series (Beal et al. 2015). First, a vertically continuous velocity profile is created for each mooring by applying a spline fit to the discrete current velocity measurements. To extrapolate to the surface, we assume a constant shear, taken over the top 50 m of ADCP data. Once continuous profiles have been constructed, linear interpolation is used in the horizontal.

Offshore of mooring G, full-depth velocity profiles are derived using current- and pressure-recording inverted echosounders (CPIES; section 2c). The geostrophic velocity profile derived from each CPIES pair is assumed to represent the velocity halfway between the instruments, enabling us to retain the higher-resolution estimate at mooring G. Linear interpolation is used in the horizontal. From the midpoint of P4 and P5 to 300 km offshore, we assume that the velocities are constant

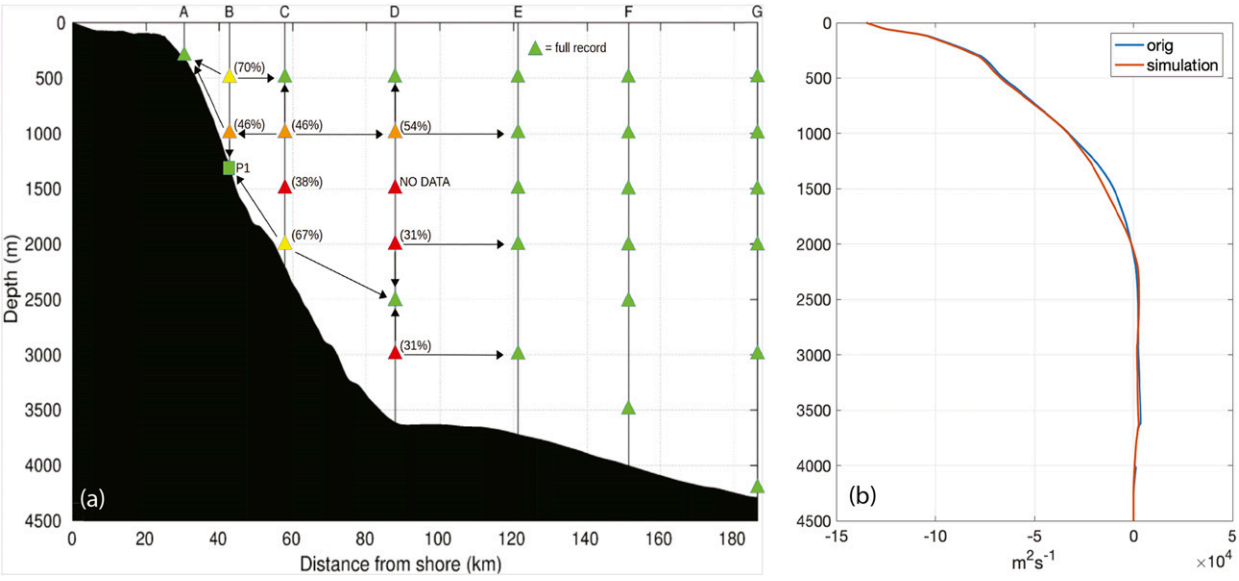

FIG. 2. ADCPs and current-meter data gaps and resulting biases: (a) Record lengths of instruments. Colors correspond to the approximate amount of time that each instrument recorded data. Arrows show neighboring instruments that were used to fill short records through linear regression. (b) Time-mean transport per unit depth profile from the ACT data ("orig"; blue) and from the simulation with shortened records ("simulation"; red).

and equal to the velocity profile derived from CPIES pair P4 and P5.

b. Temperature data

Full-length records of temperature, conductivity, and pressure at 20-min sampling intervals were recovered from 56 of the 61 deployed unpumped SBE 37 SMP microCATs (Fig. 1; https://accession.nodc.noaa.gov/0210643). Prior to vertical and horizontal interpolation, all microCAT records were quality controlled to remove spikes. For each instrument, data points more than 10 standard deviations from the mean of that instrument's record were removed. Visual quality control was conducted by comparing the records with a temperature–salinity plot of Argo and hydrographic data in the region. Records were 40-h low-pass filtered to remove tidal and inertial variability and then were 20-h subsampled.

Sea surface temperature (SST) was taken from the Group for High Resolution Sea Surface Temperature (GHRSST) Multi Product Ensemble (GMPE) (Martin et al. 2012). This data product, available daily on a 0.25° × 0.25° grid, consists of the median measurement from 11 gridded sea surface foundation temperature products.

To interpolate temperature measurements to the same regularly spaced grid as the velocity measurements, we first vertically interpolate by constructing a seasonally varying profile of

$$\frac{\partial T}{\partial P}(T)$$

using 2893 Argo and shipboard CTD profiles within 300 km of the coastline (Fig. 3a; black markers in inset), following Fillenbaum et al. (1997) and Johns et al. (2005). Between two instrument depths, the temperature is taken as a weighted mean of the integration of

$$\frac{\partial T}{\partial P}(T)$$

from the measurements above and below that grid point:

$$T(P) = \sum_{n=1}^{2} w_i \left[T(P_i) + \int_{P_i}^{P} \frac{\partial T}{\partial P}(T)\, dP \right], \tag{1}$$

where

$$w_i = 1 - \frac{|P - P_i|}{P_2 - P_1},$$

T is temperature at a grid point, P is pressure at a grid point, and P_i are the measured pressures of the instruments above and below each grid point at each point in time. Above the shallowest instrument on each mooring, SST from satellite measurements is used. Below the deepest instrument on each mooring, the

$$\frac{\partial T}{\partial P}(T)$$

relationship is integrated downward, with no weighted average [i.e., Eq. (1) is used with the summation over $n = 1$, with $w_1 = 1$]. After constructing a continuous vertical profile at each mooring at each point in time, we linearly interpolate in the horizontal.

Inshore of mooring A, the temperature is extrapolated by assuming that the time-varying horizontal SST gradient between mooring A and each point inshore of mooring A is

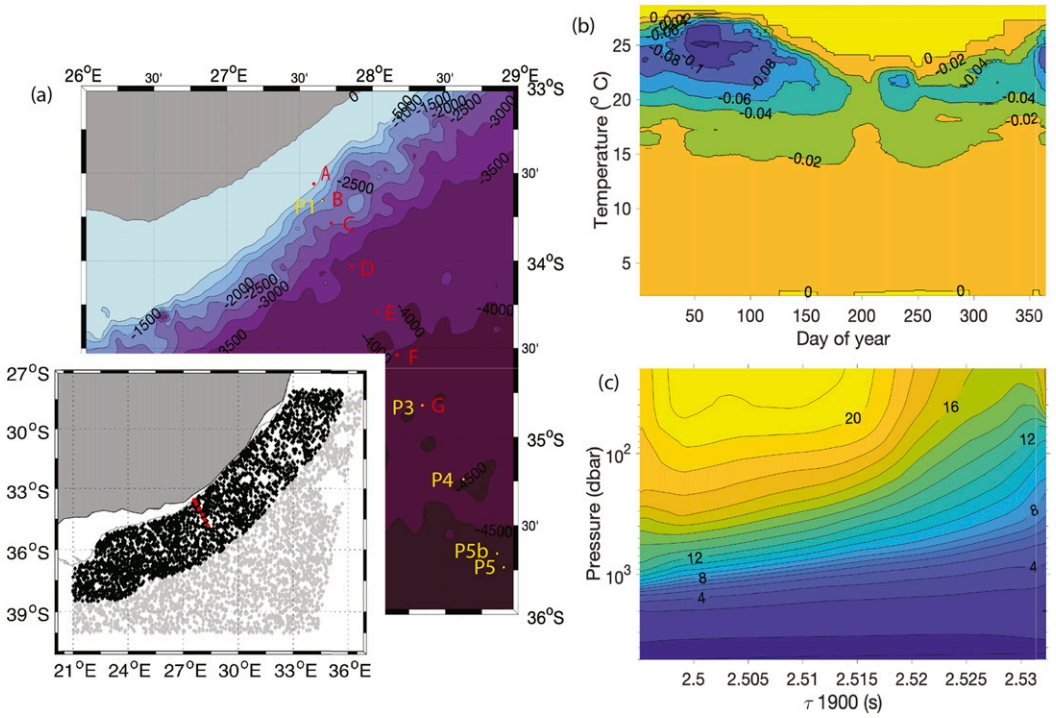

FIG. 3. (a) The locations of moorings A–G (red) and CPIES P1–P5 (yellow). Contours show the bathymetry every 500 m. The African coastline is in gray. The inset map shows a larger region with mooring locations (red), the locations of CTD/Argo profiles used to vertically interpolate temperature (black), and the locations of CTD/Argo profiles used to determine the CPIES GEM (black and gray). (b) The seasonally varying dT/dP relationship (°C dbar^{-1}) as a function of day of year and temperature. Labeled contours correspond to color fill. (c) The temperature GEM (°C) as a function of τ_{index}, the acoustic travel time at a reference depth of 1900 dbar. Labeled contours correspond to color fill. Note that the pressure is shown in logarithmic scale.

constant from the surface to the seabed. Offshore of mooring G, temperature is derived from the CPIES measurements (section 2c). Last, potential temperature is calculated using the TEOS-10 MATLAB package (McDougall and Barker 2011). All written references to ''temperature'' in this paper are potential (rather than in situ) temperature, which is represented by the symbol θ. Salinity measurements and transports are reported in a separate paper (Gunn et al. 2020).

c. *CPIES data*

CPIES data (https://accession.nodc.noaa.gov/0209237) are processed using previously established methods (Donohue et al. 2010; Beal et al. 2015). Here we give an overview; readers are referred to Beal et al. (2015) for processing details and for a comparison of CPIES and current-meter-derived velocities in the Agulhas Current.

CPIES measure three quantities: acoustic round-trip travel time from the seafloor to the ocean surface, bottom pressure, and near-bottom velocity. From these data, full water column profiles of temperature and salinity can be derived from a single CPIES instrument, and profiles of geostrophic velocity can be derived from each pair of CPIES. To do this, hydrographic data in the vicinity of the study region are used to generate lookup tables of temperature, salinity, and specific volume anomaly profiles as a function of acoustic round-trip travel time τ. This is called the gravest empirical mode (GEM) field (Meinen and Watts 2000) and allows for the generation of time series of temperature, salinity, and specific volume anomaly profiles from τ. The CPIES pressure record is used to remove the contribution of mass loading from measured τ. To derive volume transport, specific volume anomalies are integrated over pressure intervals to give time series of geopotential anomaly profiles at the location of each CPIES, and geostrophic velocities are obtained from the difference of the geopotential anomaly profiles at two adjacent CPIES referenced to their averaged near-bottom velocity records.

To create the GEM lookup table, we use 3564 CTD and Argo profiles in the region 28°–40°S, 21°–37°E (Fig. 3a, inset). This region is larger than that used to construct the $\partial T/\partial P$ relationship because the CPIES are located farther offshore than the tall moorings. The measured τ is then converted to a travel time index at 1900 dbar through a five-step process: (i) removal of the nonsteric contribution of the travel time from the pressure record, (ii) conversion to dynamic travel time, (iii) removal of the seasonal cycle, (iv) removal of the deep offset of travel time from CPIES pressure level to deep common pressure level (3800 dbar), and (v) conversion from deep pressure level to common pressure level (1900 dbar). Using the travel

time at the common pressure level and the GEM, we derive temperature and salinity profiles from each CPIES and velocity profiles from each CPIES pair.

The GEM method uses deseasoned profiles. In section 2d, we test the impact of retaining the seasonal cycle in the profiles and find that residual errors are larger when profiles are not deseasoned. However, regardless of the treatment of seasonality, large errors of 0.5°–2°C remain in the CPIES-derived near surface temperatures. The seasonal cycle of temperature extends to 200 dbar, based upon hydrographic data in the region. Therefore, we discard the upper 200 dbar of the CPIES-derived temperature profiles and linearly interpolate between the 200-dbar CPIES-derived temperature and the SST. Considering the expected error of 0.4°C from GMPE SST (Martin et al. 2012), we expect this to reduce errors as compared with retaining the CPIES-derived upper-200-dbar temperatures.

Data from instruments P1 and P5b are not used here. P1 was located inshore, near tall moorings with better vertical resolution of temperature and current velocity. P5b was located within 10 km of P5 and the records are highly correlated (Pearson's correlation of 0.99 for 200-dbar temperature). Using P5b instead of P5 does not change any results.

d. GEM sensitivity

The accuracy of the derived temperature and velocity profiles from the CPIES relies on appropriate choices of which data to include in the GEM. For instance, the relationship between acoustic travel time and temperature may be different on the inshore and offshore sides of the current. To ensure our results are robust, we tested the sensitivity of using different reasonable GEM choices. We tested four setups: (i) the method described in section 2c and used by Beal et al. (2015), (ii) a GEM restricted to using data within 300 km of the African coastline, (iii) a GEM using profiles that were not deseasoned, and (iv) a GEM with a shallower reference level of 1400 dbar. We find that these differing GEMs have little impact on the estimated temperature and velocity fields. The largest difference is caused by restricting the data used to construct the GEM to within 300 km of the coastline, and it reduces the transport between P4 and P5 by 0.27 Sv, well below the estimated CPIES error (section 3a). Other studies have similarly found that the GEM method is relatively insensitive to the region used for the GEM database (Kersalé et al. 2019).

e. Definitions

Previous studies have focused on the volume transport of the Agulhas Current, defined as

$$\iint v\,dx\,dz, \tag{2}$$

where v is the cross-track velocity. Temperature transport is defined similarly but requires additional measurements of temperature:

$$\iint \rho C_p v\theta\,dx\,dz, \tag{3}$$

TABLE 1. Summary of estimated errors. Boldface type indicates the final errors as stated in the results and conclusions.

Velocity instrumental error	1.0 cm s^{-1}
ADCP and current-meter sampling error	5.5 Sv
CPIES volume transport error	13.5 Sv
Box volume transport error (20 h)	5.7 Sv
Box volume transport error (mean)	**4 Sv**
Jet volume transport error (20 h)	14.6 Sv
Jet volume transport error (mean)	**11 Sv**
MicroCAT sampling error	0.23°C
Temperature-derived error	0.07 PW
Box transport-derived error	0.12 PW
Box temperature transport error (20 h)	0.14 PW
Box temperature transport error (mean)	**0.1 PW**
Jet transport-derived error	0.28 PW
Jet temperature transport error (20 h)	0.28 PW
Jet temperature transport error (mean)	**0.2 PW**

where ρ is density, C_p is the specific heat capacity of seawater, and θ is potential temperature; ρC_p is taken as the constant value of 4.093 J K^{-1} cm^{-3} (Hall and Bryden 1982). The temperature transport can change due to changes in velocity, temperature, or the covariance of the two quantities. Because this calculation does not conserve mass, the absolute value of the temperature transport depends on the reference temperature (0°C in this paper). We follow previous authors and refer to the result of Eq. (3) as "temperature transport" rather than "heat transport" to reflect that mass is not conserved and absolute values are arbitrary (Hall and Bryden 1982).

To quantify the transport of the Agulhas Current, we need to define its boundaries [the limits of integration of Eqs. (2) and (3)]. Following Beal et al. (2015), we define the Agulhas Current in a boundary layer ("box") sense as well as a streamwise ("jet") sense. The box transport is equal to the net transport (northward and southward) integrated from the coast to 219 km offshore. The jet transport consists of only southward transport from the coast to the first maximum of cumulative transport more than 110 km offshore. Southward velocities and transports are defined as negative.

We define current meanders as any time that the sea level anomaly (SLA) near mooring C (33.6°S, 28°E) from the along-track product distributed by Copernicus Marine Environment Monitoring Service is below −0.2 m, following Elipot and Beal (2015). There were five meanders during the 25-month period of ASCA (an average of 2.4 yr^{-1}), higher than the mean of 1.6 meanders per year from 1993 to 2013 (Elipot and Beal 2015).

3. Errors

We first quantify the velocity and volume transport errors, then we quantify the temperature errors, and then last we combine these errors to obtain the temperature transport errors (Table 1).

a. Velocity and volume transport errors

There are four sources of velocity error. First, there are instrumental errors associated with the current meters and ADCPs. Second, there is a sampling error from the interpolation between the velocity measurements, based on the array

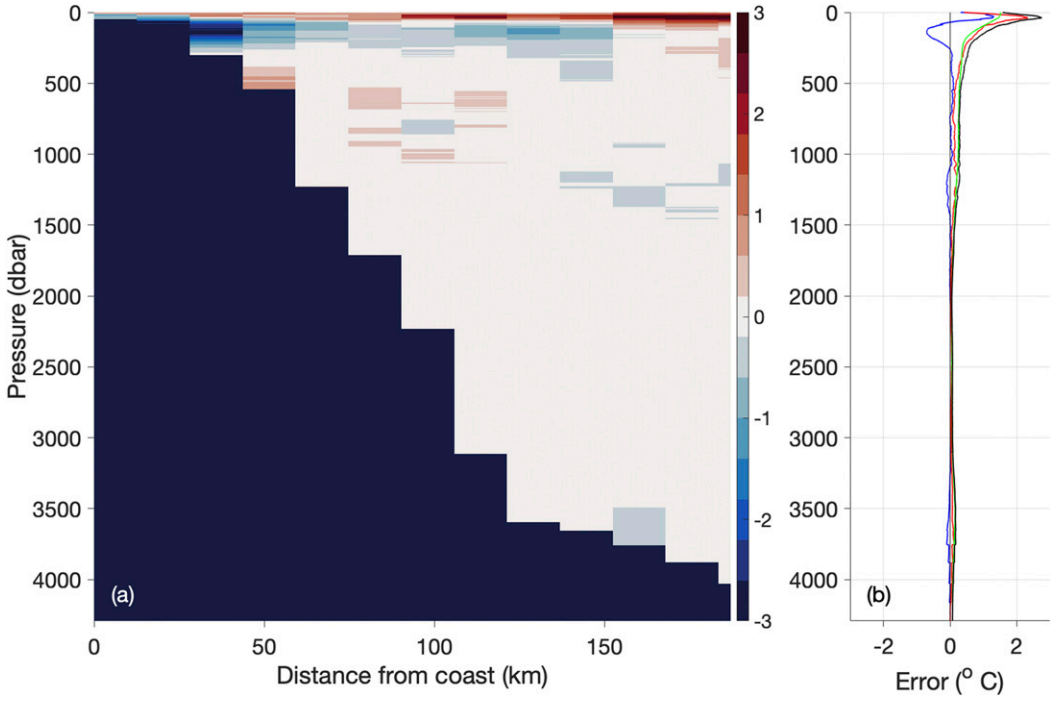

FIG. 4. Temperature error fields and vertical profile: (a) Mean error field (°C), constructed by subsampling three hydrographic crossings of the Agulhas Current to the locations of ASCA temperature measurements, re-interpolating the data, and subtracting them from the high-resolution hydrographic "truth." (b) Mean depth profile of the errors. Root-mean-square sampling error is shown in red, and sampling bias is in blue. CPIES method error is shown in green. Combined sampling and CPIES root-mean-square error is shown in black.

instrumental configuration. Third, there is an error associated with the GEM method used to derive velocity profiles from CPIES. Last, there is an error due to the missing data from instruments that did not record for the full 25 month mooring deployment, which we consider separately from the sampling error.

Current-meter and ADCP instrumental errors are estimated using the power spectra of the time series of each instrument. The background white noise level is taken as the instrumental error. This ranges from 0.03 to 4.7 cm s^{-1}, with a median of 1.0 cm s^{-1}. These errors are similar in magnitude to those found during ACT (Beal et al. 2015).

The velocity sampling error was estimated using optimal interpolation, as in Beal et al. (2015). The error on each 20-h estimate across the tall mooring section is 5.5 Sv. Adding the instrumental error to this yields a total error of 5.7 Sv. This error applies to the "box transport" definition that is almost entirely covered by the tall moorings that extend 187 km offshore.

The jet transport definition sometimes extends more than 219 km offshore, and so it also contains errors from the CPIES. The errors in velocity from the CPIES were estimated by Beal et al. (2015), who estimate a formal error of 13.5 Sv on low-pass-filtered, 20-h subsampled estimates. We use the same error estimate, which is appropriate because we are in the same region and using a similar instrument configuration. Added in quadrature to the 5.7-Sv error from the tall moorings yields a total jet volume transport error of 14.6 Sv.

b. *Temperature errors*

Errors in temperature are due to microCAT instrument errors, a sampling error, and the CPIES methodological error in deriving temperature profiles. The microCATs were calibrated by the manufacturer before deployment, and have a stated accuracy of 0.002°C. We tested for sensor drift by conducting postdeployment calibration dips (https://accession.nodc.noaa.gov/0209235) on a dual-sensor CTD package (Kanzow et al. 2006). After calibration, 43 instruments agreed with the CTD to within 0.002°C, the WOCE standard for measurements of temperature (Joyce 1988). Thirteen instruments did not meet this standard, with a maximum error of 0.003°C. These instrumental errors are two orders of magnitude smaller than the estimated sampling errors and are not considered further.

Sampling errors due to the temperature interpolation are evaluated using three hydrographic crossings of the Agulhas Current at 34°S, in 2010, 2011, and 2013. Each high-resolution hydrographic section is subsampled to the location and mean depths of the microCATs. The full temperature field is then reconstructed using our temperature interpolation method (section 2b), and the difference between the hydrographic section "truth" and the subsampled and interpolated product is taken as the sampling error (Fig. 4). RMS errors in the upper 500 dbar are large (spatial mean of 0.67°C) because of the low number of instruments in the upper ocean. Averaged over the entire array area, the RMS error is 0.14°C.

The CPIES GEM methodological error can be estimated at each depth by considering the residuals between the data and the GEM function fit to the data. For temperature, these errors vary from 0.44°C at 200 dbar to 0.066°C at 4500 dbar (green line in Fig. 4b). Adding the CPIES methodological error profile to the microCAT sampling error profile in quadrature yields a total RMS error over the array of 0.23°C (0.91°C in the upper 500 m).

c. Bias errors

We now investigate any possible bias in the volume and temperature transport. We estimate the error due to the missing velocity records using data from the second deployment (2011–13) of ACT, which had a very similar arrangement of current meters and ADCPs as ASCA but no data failures (Beal et al. 2015). We run a simulation using the ACT data, where we remove data at the times and locations of instrument failure during ASCA. Then, the data gaps are filled using the same multiple regression models used in ASCA (Fig. 2a). In comparing the true ACT volume transport with the simulated transport with data gaps, it is seen that the simulated transport is biased too strong southward by 3.7 Sv (corresponding to 0.18 PW based on the transport-weighted temperature), due to an overestimation of southward velocities between 1000- and 2000-m depth (Fig. 2b). Nevertheless, the time series of the simulation and the ACT truth are highly correlated (Pearson's correlation of 0.99), and we can be confident that the ASCA array accurately captures the variability of the volume transport. While we note this possible bias, we do not correct for it in our absolute transports. The variance of the second ACT time series, with no current meanders, is very different from that of ASCA and so we cannot be certain of the simulated bias.

A hydrographic section was conducted in July 2016 (https://doi.org/10.15493/SAEON.EGAGASINI.24000008), which we use to assess a possible bias due to the lack of temperature recording instruments in the upper ocean. The gridded mooring data are on average 0.06°C cooler than the hydrographic data, with larger biases near the surface where the mixed layer is not well resolved by the moorings. The resulting transport-weighted temperature bias is −0.35°C and the temperature transport bias is −0.11 PW. We correct for this by adding these constant values to the time series of temperature transport and transport-weighted temperature.

d. Temperature transport errors

To determine an error for temperature transport, we follow the method of McDonagh et al. (2015). First, we consider how the error in temperature propagates into the temperature transport calculation, called the temperature-derived error. Next, we consider how the error in volume transport propagates into the temperature transport calculation, that is, the transport-derived error. We then combine these two error sources in quadrature.

The temperature-derived error, $\sigma_T = V\delta\theta$, is calculated by multiplying the spatial and temporal mean volume transport V by the temperature error $\delta\theta$. Multiplying the mean volume transport by the 0.23°C temperature error yields a temperature-derived error of 0.07 PW.

The transport-derived error, $\sigma_v = \theta\delta V$, is the mean temperature θ multiplied by the volume transport error δV. For the box definition, the volume transport error is 5.7 Sv. We multiply this by the mean temperature across the array to calculate a transport-derived error of 0.12 PW. Adding this in quadrature to the temperature-derived error yields a box temperature transport error of 0.14 PW. For the jet temperature transport, the volume transport error is 14.6 Sv, leading to a transport-derived error of 0.28 PW. Added in quadrature to the 0.07-PW temperature-derived error, this yields a jet temperature transport error of 0.28 PW.

To calculate errors on the mean, we divide the 20-h error estimates by the square root of the degrees of freedom, using the observed 8-day (box) and 10-day (jet) decorrelation time scales. The box instrumental errors on the mean are then 0.6 Sv and 0.02 PW. For the jet errors, only the barotropic part of the CPIES error is random (Beal et al. 2015), and so the jet transport instrumental error on the mean reduces to 8.9-Sv error and 0.17 PW. We then add these to the statistical error, using the standard error of the mean, following Kanzow et al. (2010). The total errors on the time mean are 4 Sv and 0.1 PW (box) and 11 Sv and 0.2 PW (jet). The largest error as a percent of the time-mean signal is the 14% error on the jet volume transport.

4. Results

a. Temperature and velocity structures

Because of the strong impact of meanders on the temperature and velocity structure of the current, we construct mean fields during meander and nonmeander times (Fig. 5). Meanders occur during 8.3% of the time series, in five separate meander events (Fig. 5c). These meanders range from 4 to 17 days in duration, with an average of 12 days.

In the nonmeander mean, the core of the current is 31 km offshore with a peak speed of $-1.77\ \mathrm{m\,s^{-1}}$. The current extends 211 km offshore at the surface and to pressure levels of 2000–3000 dbar with weak northward velocities below. The isotherms slope upward toward the coast, reflecting the southward geostrophic current.

In the meander mean, the current is slower and broader. The core of the current is 151 km offshore, with a peak speed of $-0.91\ \mathrm{m\,s^{-1}}$. This peak speed is biased low, as the core of the current moves horizontally during a meander. Nonetheless, a streamwise composite of meanders and nonmeanders (noisier and not shown) confirms that the peak speed is slower (-1.26 vs $-1.92\ \mathrm{m\,s^{-1}}$), and the current is wider (226 vs 204.5 km) during meanders than during nonmeanders, in agreement with Leber and Beal (2014). During meanders, the isotherms slope upward toward the coast where there is southward flow, and then slope downward inshore of the southward flow where a weak northward counter flow exists. The thermocline on the offshore side of the current is at approximately 1000-m depth during both meanders and nonmeanders. An animation of the temperature and velocity fields at 20-h time steps is available in the online supplemental material.

b. Volume and temperature transports

To investigate variability in the integrated current transports, we calculate time series of the volume and temperature

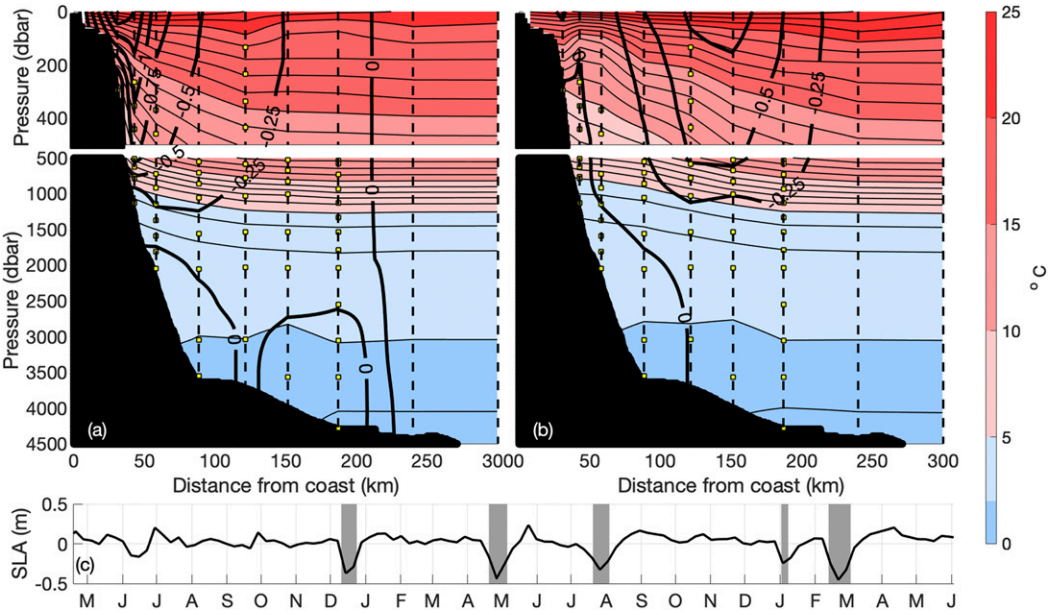

FIG. 5. Mean temperature (°C) and velocity ($m\,s^{-1}$) structure of the Agulhas Current during (a) nonmeandering times and (b) meandering times. Colors and thin contours show temperature, with each contour corresponding to 1°C. Thick contours show cross track velocity, with each contour corresponding to $0.25\,m\,s^{-1}$. (c) Meander time series, as measured by sea level anomaly at 33.6°S, 28°E. Meanders are defined as times during which the SLA is lower than −0.2 m (gray shading).

transports (Fig. 6). The volume and temperature time series are highly correlated with each other ($r = 0.96$ for box definition; $r = 0.95$ for jet definition, where r is the Pearson's correlation) (Fig. 6). The mean box volume transport is -75 ± 4 Sv and the jet volume transport is -76 ± 11 Sv, which are not statistically different than the volume transports from ACT (-76 ± 5 Sv and -84 ± 11 Sv, respectively; Beal et al. 2015). The mean box temperature transport is -3.8 ± 0.1 PW, and the mean jet temperature transport is -3.8 ± 0.2 PW (relative to 0°C). This is larger than the 2.48-PW temperature transport of

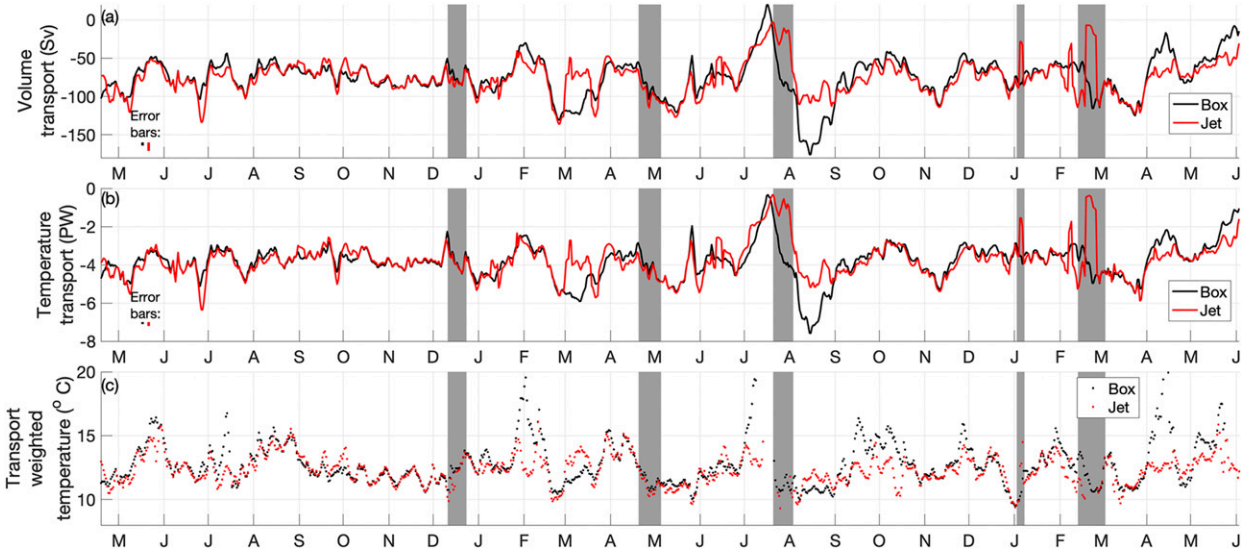

FIG. 6. (a) Time series of the volume transport of the Agulhas Current. The boundary layer ("box") transport is in black, and the streamwise ("jet") transport is in red. Sizes of errors on each 20-h estimate are shown near the left axis. (b) Time series of the temperature transport. (c) Time series of the transport-weighted temperature, only shown when volume transport is larger than 25 Sv southward. Gray shadings in (a)–(c) show periods during which the current is meandering.

TABLE 2. Statistics of the volume and temperature transport of the Agulhas Current.

	Jet volume transport (Sv)	Box volume transport (Sv)	Jet temperature transport (PW)	Box temperature transport (PW)	Jet transport-weighted temperature (°C)	Box transport-weighted temperature (°C)
Mean	−76	−75	−3.8	−3.8	12.3	12.7
Std dev	22	26	0.9	0.9	1.2	1.7
Min (poleward)	−3	20	−0.3	−0.3	9.3	9.5
Max (poleward)	−136	−176	−6.4	−7.6	16.1	19.9
Median	−75	−74	−3.8	−3.7	12.3	12.4
Meander mean	−66	−82	−3.1	−3.9	11.5	11.6
Nonmeander mean	−77	−75	−3.8	−3.8	12.4	12.1

the Florida Current or the 1.79-PW temperature transport of the Kuroshio, both relative to 0°C (Molinari et al. 1990; Zhang et al. 2002).

The volume and temperature transport time series are highly variable, with standard deviations of 22 Sv and 0.9 PW (jet) and 26 Sv and 0.9 PW (box). The variability is larger using the box definition, likely because this integration sometimes misses the core of the Agulhas jet entirely. Using the jet definition, the transport varies from almost zero southward transport to −136 Sv transporting −6.3 PW. In July 2017, when the transport was near zero, sea surface height shows that the current meandered so far offshore that it was not wholly captured by the mooring array (not shown). The statistics of these time series are summarized in Table 2.

To investigate the relationship between temperature transport and the temperature and velocity cross sections, we plot composites of temperature and velocity during the 10% strongest southward box temperature transport times, and during the 10% weakest times, excluding meanders (Fig. 7). The difference of the two fields shows cold temperature anomalies from the coast to 100 km offshore, and warm anomalies from 150 to 300 km offshore, with a maximum near 220 km offshore at 1000-m depth. This temperature anomaly pattern is indicative of a shoaling of isotherms inshore, and a deepening of isotherms offshore, which steepens the isotherm slope. The difference of the two composites shows southward velocity anomalies at all depths from the coast to 250 km offshore (thick contours in Fig. 7c), consistent with a deepening and broadening of the current as it strengthens. The increased southward velocities are consistent with the increased isotherm slope through geostrophy. This deepening and broadening mode of the current can largely be explained by the square of the difference in upper-layer thickness across the current (Fig. 7d), which we return to in section 4e.

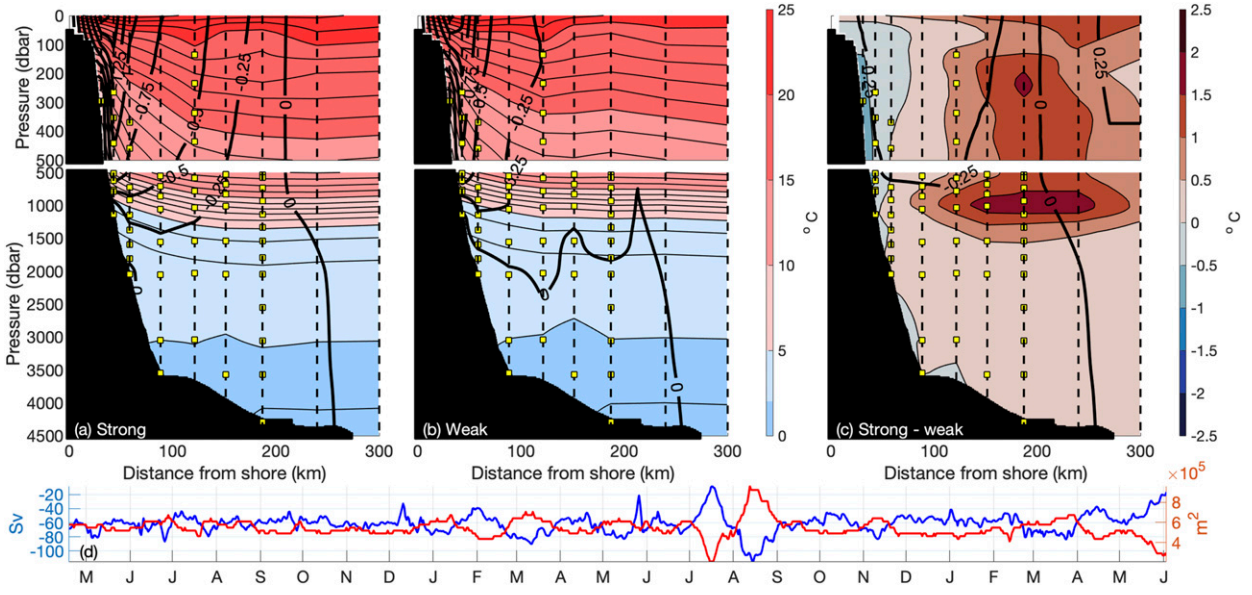

FIG. 7. (a) Composite temperature (colors) and velocity (thick contours) of the strongest 10% of southward box temperature transport times, excluding meander times. (b) Composite of the weakest 10% of southward box temperature transport times, excluding meander times. (c) The difference between the composites of strong minus weak temperature transport. (d) Time series of the box volume transport above 1000 m [Sv; blue (left axis)] and the square of the difference of depth between the 10°C isotherm at 20 km and at 219 km offshore [m^2; red (right axis)].

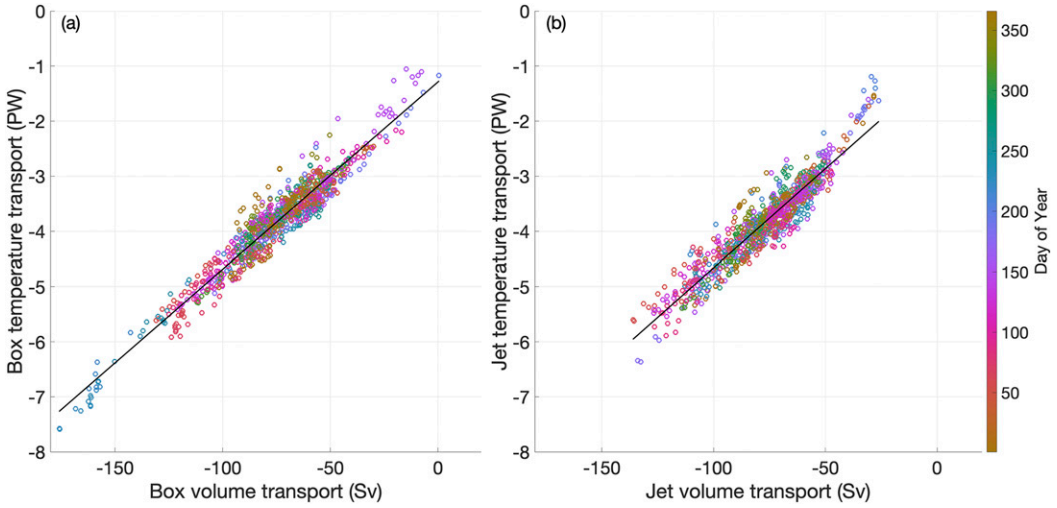

FIG. 8. (a) Scatterplots of the (a) box and (b) jet temperature vs volume transport. Colors show the day of year of each data point. The black line shows a linear fit of the two variables.

c. Transport-weighted temperature

Next, we quantify the time-varying transport-weighted temperature, defined as

$$\frac{\iint v\theta \, dx \, dz}{\iint v \, dx \, dz}. \tag{4}$$

Multiplying the volume transport by the transport-weighted temperature yields the temperature transport, and so the transport-weighted temperature can be used to convert between the two transport quantities. We show both the box and jet definitions of the transport-weighted temperature (Fig. 6c); however, the box definition is undefined in July 2017 when the volume transport goes to zero. Hence, we only calculate the transport-weighted temperature when the southward volume transport is greater than 25 Sv.

The mean transport-weighted temperatures are 12.3°C (jet) and 12.7°C (box), with standard deviations of 1.2° and 1.7°C, respectively (Fig. 6c). The box transport-weighted temperature is 1.1°C cooler than estimated previously from a single hydrographic section at 32°S (Beal and Bryden 1999), but within one standard deviation. Cooler temperatures (e.g., heat loss to the atmosphere) might be expected at the ASCA array that is located farther poleward at 34°S, yet the difference could also be due to temporal variability. The temporal variability of the transport-weighted temperature in the Agulhas is far higher than in the Florida Current, with a range of 9.5°–19.9°C, as compared with 18°–21°C (Shoosmith et al. 2005). No statistically significant seasonal cycle is observed. Some of the variability in the transport-weighted temperature is related to meandering. However, considering that meandering cools the current by only 0.9°C while the range of the transport-weighted temperature is more than 10°C, most variability is unrelated to meanders.

Temperature transports in the ocean are typically strongly related to volume transport and the Agulhas is no exception, with $R^2 > 0.9$ for both jet and box (where R^2 is the coefficient of determination for the corresponding linear regression model) (Fig. 8). A similar relationship in the Florida Current means that temperature transport there is estimated using volume transport from the multidecadal cable time series and a constant transport-weighted temperature with an RMS error of 0.11 PW (Shoosmith et al. 2005). Yet for the Agulhas, the residuals from the linear fits are large due to the high variability in the transport-weighted temperature, resulting in RMS errors of 0.24 and 0.27 PW for box and jet, respectively. Including a seasonal variation does not improve these statistics.

The transport-weighted temperature tends to be cooler when volume transport is larger, although the relationship is nonlinear (Fig. 9). This is consistent with the composites in Fig. 7, which show a deeper and broader current during times of strong transports. When the current deepens, it transports cooler waters, cooling the transport-weighted temperature. The relationship may be nonlinear because the current can only deepen to the seabed; beyond that point, stronger volume transports cannot continue to deepen the current. Using the jet definition, the relationship breaks down for transports of less than 40 Sv. This may be because the offshore edge of the current is not well constrained during these weak volume transport times, complicating the jet definition of the current. For example, in July 2017 the current meandered far enough offshore that it is not fully captured by the mooring array. No seasonal cycle is observed in the relationship between volume transport and transport-weighted temperature.

The cooler transport-weighted temperatures at times of stronger volume transport may explain the lack of observed seasonal cycle in the temperature transport. In austral summer, the southward volume transport increases (Beal et al. 2015). Based on Fig. 9, we hypothesize that the transport-weighted temperature cools due to the deepening and broadening of the current associated with its seasonal strengthening. This may offset the effect of the larger volume transport on the

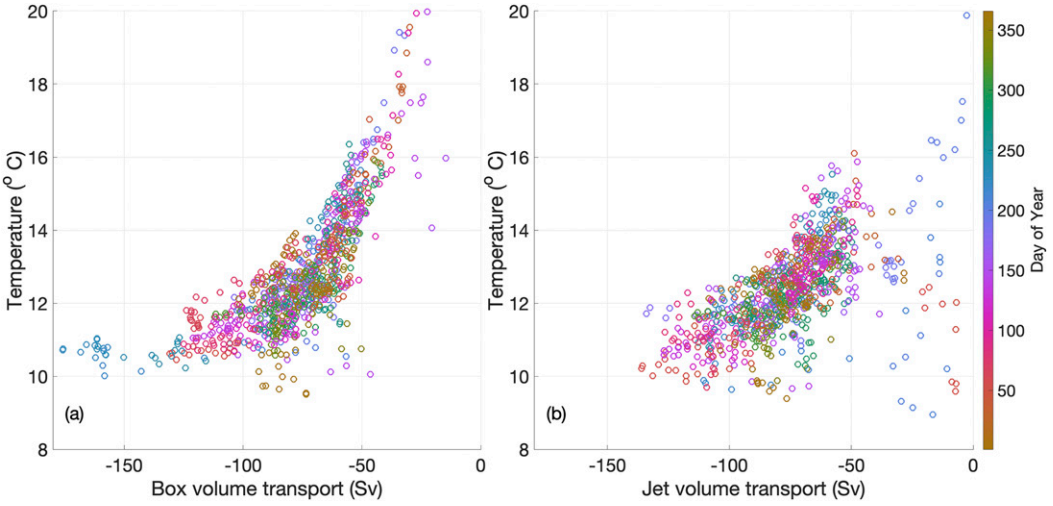

FIG. 9. (a) Scatterplots of the (a) box and (b) jet volume transport vs transport-weighted temperature. Colors show the day of year of each data point.

temperature transport. A longer time series would be needed to confirm this hypothesis, as no seasonal signal is seen is Fig. 9 or in the transport-weighted temperature.

d. Modes of temperature variability

To further investigate the variability in the temperature cross section and its relationship to the volume and temperature transports, we conduct an EOF analysis over the entire array area after detrending all time series. An EOF analysis decomposes the variability of the temperature field into orthogonal modes, with the first mode describing the most variance. EOFs do not necessarily describe physical processes, but by linking the EOF modes to the previously presented analysis, we can quantify the variability caused by different processes. Correlations are expressed as r, the Pearson's correlation, and correlations above 0.23 are significant at the 95% threshold using a decorrelation time scale of 10 days (calculated jet transport decorrelation time scale).

We find that the EOFs of the velocity field (not shown) are very similar to the previously described modes of velocity variability (Elipot and Beal 2015). The first three modes correspond to current meandering, with no significant impact on the integrated volume transport. The fourth mode is correlated with full current volume transport. Complex EOFs can describe current meandering in a single mode (Elipot and Beal 2015). Combined EOFs of temperature and velocity are similar to the temperature EOFs presented below, but with meandering represented by the first two modes (not shown).

Meanders drive the largest amount of variability in the temperature cross section. The first EOF (Fig. 10a) explains 40% of the variance in temperature and the corresponding principal component time series (Fig. 11a) is highly correlated with the meander time series ($r = 0.84$). During a meander, EOF 1 is in a negative phase, and therefore meandering results in a cooling near shore, and a surface confined warming offshore. Temperature anomalies associated with meanders can be calculated by multiplying the value of the principal component time series during a meander by the pattern of EOF 1. Maximum temperature anomalies are −4°C, located about 60 km offshore during strong meanders. The maximum temperature anomalies occur from 100- to 1500-m depth, where Subtropical Surface Water, South Indian Central Water, and Antarctic Intermediate Water are found [water mass definitions from Beal et al. (2006)]. This is broadly in agreement with Leber et al. (2017), who found maximum cooling of 9°C during a single meander due to upward displacement of central waters. The first principal component time series is not significantly correlated with the box temperature transport ($r = -0.20$) and has a significant but modest negative correlation with the jet temperature transport ($r = -0.43$). Meandering can explain some variability in the temperature transport, but much variability is unrelated to meanders.

Variability in the temperature transport is best explained by a steepening of isotherms associated with a deepening and broadening of the current, consistent with the composites shown in Fig. 7. The second EOF explains 25% of the variance in temperature (Fig. 10b, principal component time series in Fig. 11b), and the second principal component time series is significantly correlated with the temperature transport time series ($r = -0.72$ for box; $r = -0.51$ for jet). This mode is also significantly correlated with the volume transport of the current ($r = -0.68$ for box; $r = -0.51$ for jet). When southward temperature (and volume) transport increases, this mode shows cool temperature anomalies near the current core, and warm temperature anomalies on the offshore flank of the current. Maximum temperature anomalies occur within Subtropical Surface Water and South Indian Central Water. The temperature variability described by EOF 2 is correlated pointwise with southward velocity anomalies on the offshore flank of the current, 100–200 km offshore, extending from the surface to the seabed (Fig. 10d), as would be expected from geostrophy.

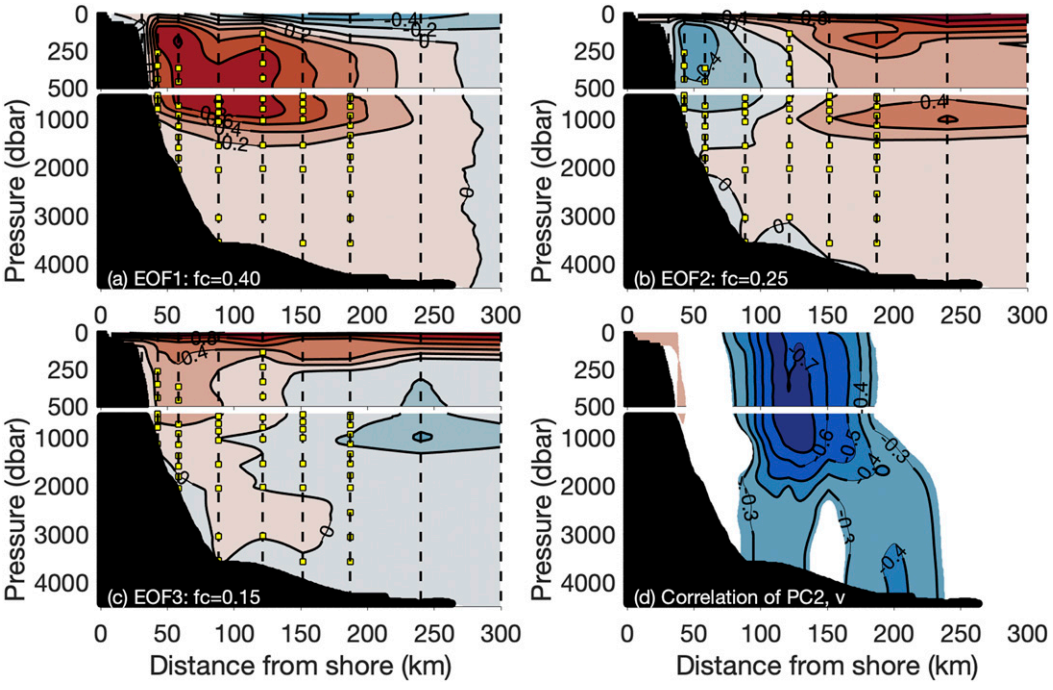

FIG. 10. The first three EOFs of the temperature field, labeled with the fraction of the total variance that each mode explains (fractional covariance; "fc"). The corresponding principal component time series are shown in Fig. 11, below. (a) The first EOF of the temperature field, describing 40% of the variance. (b) The second EOF of the temperature field, describing 25% of the variance. (c) The third EOF of the temperature field, describing 15% of the variance. (d) The pointwise correlation coefficient between principal component 2 and the cross-track velocity. Negative means that the pattern shown in EOF 2 is associated with negative anomalies of velocity (increased southward velocity). Correlations of less than 0.23 are not shown because they are not significant at the 95% confidence level according to the Pearson correlation using a decorrelation time scale of 10 days.

A seasonal cycle can explain some of the remaining variability in temperature. The third EOF explains 15% of the temperature variance (Fig. 10c) and is characterized by a surface intensified warming with weak anomalies below 500 dbar. It is weakly correlated with the box temperature transport ($r = 0.35$) and not correlated with the jet temperature transport ($r = 0.05$). There is a seasonal cycle in the principal component time series, superimposed with higher frequency variability (Fig. 11c). Surface temperatures are lowest in August–September and highest in February–March, as expected for a surface flux forced seasonal cycle in the Southern Hemisphere subtropics. Maximum temperature anomalies are at the surface and reach 2°C. The seasonal cycle represented by EOF 3 extends deeper within the core of the current than it does offshore, possibly because the upward sloping isopycnals allow heat to mix deeper along isopycnals within the core of the current. The temperature anomalies from the seasonal mode are mostly restricted to the Tropical Surface Water layer, with some penetration to Subtropical Surface Water in the core of the current. This mode of variability is highly dependent on the SST data, and has a substantially different structure if SST data are omitted (not shown).

In summary, while meanders describe the most variability in the temperature cross section, deepening and broadening of the current explains more variability in the integrated temperature transport. Meanders are likely the most important process when considering SST-forced and biological impacts, due to the upwelling of cold, nutrient rich water. The current deepening and broadening may be more important for the heat budget of the full Indian Ocean, as it is most highly correlated with the temperature transport of the current. It is likely that other modes dominate the temperature and temperature transport variability on longer time scales, as has been found for the volume transport (Elipot and Beal 2018).

e. *Baroclinic and barotropic anomalies*

We have seen that the Agulhas Current and its temperature transport are highly variable. To investigate the origins of this variability, we attempt to separate barotropic and baroclinic anomalies. Barotropic anomalies will tend to approach our section from up or down stream, following the continental slope, while baroclinic anomalies will propagate into the system from the east through eddies and Rossby waves. We treat the Agulhas Current as a simplified two-layer system, with the layers divided at 1000 m, the approximate depth of the thermocline. We subtract the time-mean from all records, then take the spatial mean velocity anomalies of each layer from the coast to 220 km offshore. The upper-layer velocity anomalies are moderately correlated with the lower-layer velocity anomalies with $R^2 = 0.36$ (Fig. 12a). In other words, 36% of the

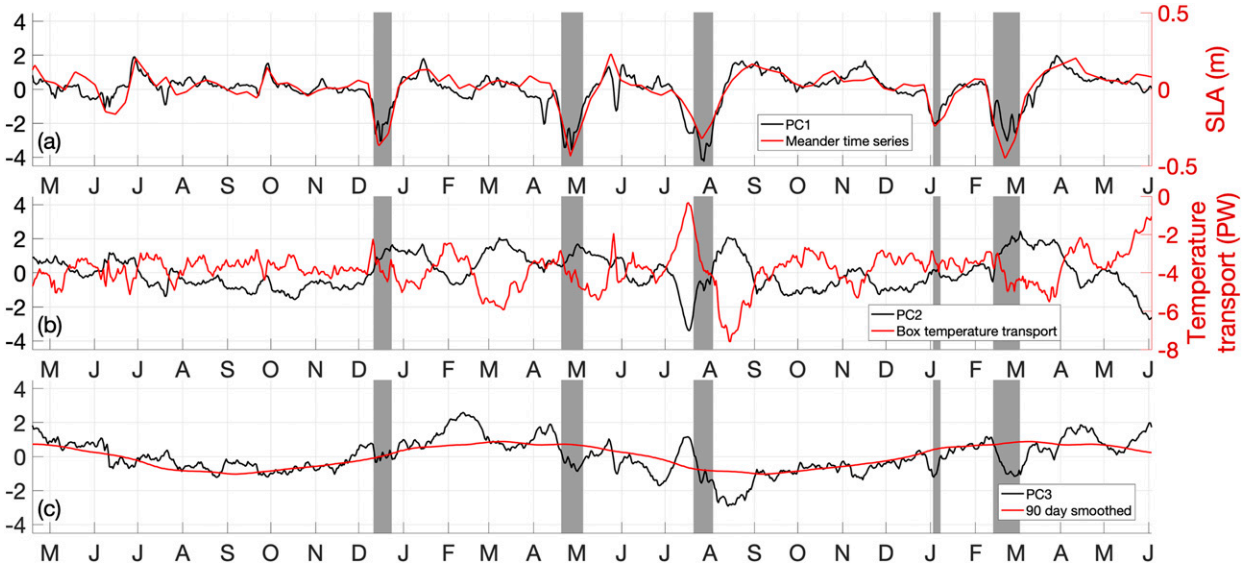

FIG. 11. The principal component time series of the first three EOFs, (a) principal component 1 (black; left axis) and the sea level anomaly near mooring C used to determine meander times (red; right axis), (b) principal component 2 (black; left axis) and the box temperature transport (red; right axis), and (c) principal component 3 (black) shown with 90-day smoothing (red) to highlight seasonal variability. Gray shadings in (a)–(c) show periods during which the current is meandering.

variance of the upper-layer velocity is related to variance in the lower-layer velocity, and they tend to vary in the same direction, illustrating that about one-third of the velocity variance is barotropic. The barotropic contribution to the velocity variance is similar during meander and nonmeander times.

Next, we divide the velocities into baroclinic and barotropic components following Andres et al. (2017). We assume that the velocity in each layer consists of a barotropic and a baroclinic component; that is, $v_{\text{upper}} = v_{\text{BT}} + v_{BC\text{upper}}$ and $v_{\text{lower}} = v_{\text{BT}} + v_{BC\text{lower}}$, with v_{BT} being the barotropic component of the velocity and v_{BC} being the baroclinic component in each layer. The barotropic velocity is calculated as the time-varying, section-averaged, vertical-mean velocity anomaly from the coast to 219 km offshore. The baroclinic velocities in each layer can then be inferred as the difference of the layer total velocity anomaly and the barotropic component.

The barotropic velocity is strongly correlated with the upper-layer velocity ($R^2 = 0.78$; Fig. 12b). In contrast, the barotropic velocity is only weakly correlated with the lower-layer velocity ($R^2 = 0.22$). This is because the lower-layer velocity anomalies are very small compared to the upper-layer velocity anomalies, and the flow is more surface intensified than can be described by the assumed barotropic and first baroclinic modes. These results are consistent with a so-called surface mode, a surface intensification of the first baroclinic mode in the presence of sloping bottom topography or a mean flow (LaCasce 2017; Brink and Pedlosky 2020). To test for this situation, we calculate the difference of the upper-layer thickness squared across the current and look for proportionality with upper-layer volume transport, assuming a 1.5-layer model as the simplest representation of a surface mode. The volume transport above 1000 m is highly correlated with the square of the difference of the depth of the 10°C isotherm at 20 and 219 km offshore, with a Pearson's correlation of 0.84 (Fig. 7d). Further, the 1.5-layer model describes 78% of the full depth temperature transport variance, because most of the temperature transport variance occurs in the upper 1000 m. Because the 1.5-layer model and the deepening and broadening mode both describe a majority of the variance in temperature transport, and both are related to the isotherm slope across the current, we hypothesize that the surface mode is the mechanism for the observed deepening and broadening of the current. The dominance of a surface mode is notably different than what is found in the Kuroshio, where a similar decomposition shows a strongly barotropic lower layer (Andres et al. 2017).

Barotropic instability has previously been linked to Agulhas Current meandering (Elipot and Beal 2015; Tsugawa and Hasumi 2010). Baroclinic instabilities may also play a role in meanders, but thus far this has not been quantified in observations. Our EOF analysis of the ASCA data suggests that baroclinic instability may be important, because the maximum of the meandering mode (EOF 1) is at 500-m depth, which is similar to the subsurface maximum in eddy available potential energy seen by Argo floats in the Agulhas Current region (Roullet et al. 2014). A surface mode is a combination of both barotropic and baroclinic modes, and so we cannot link a specific process to the dominant broadening and deepening mode of the current. A more thorough analysis of baroclinic instabilities from the ASCA dataset will be presented in a future paper.

f. Agulhas leakage heat flux

A portion of the temperature transport of the Agulhas Current quantified here enters the Atlantic Ocean through Agulhas leakage. Leakage fluxes are important to quantify

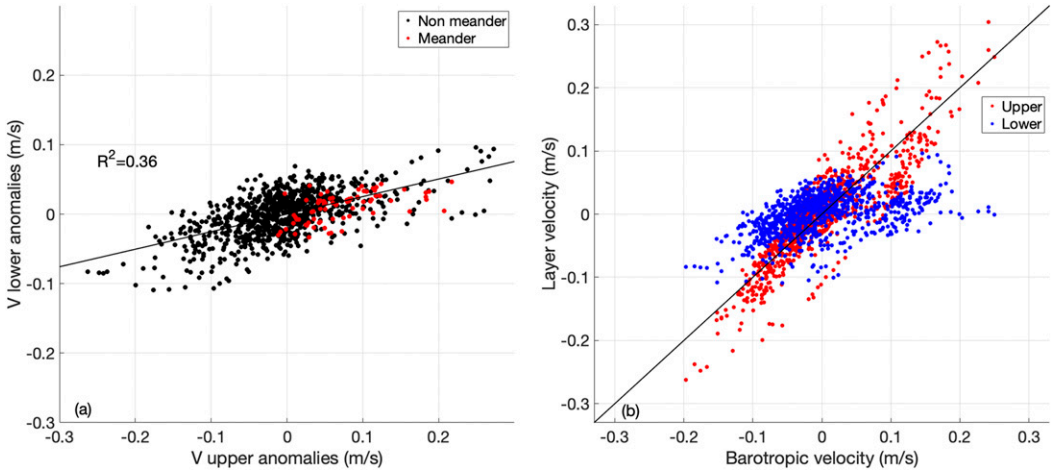

FIG. 12. (a) Scatterplot of the spatial mean 0–1000-m velocity anomaly vs the spatial mean below-1000-m velocity anomaly. Nonmeander times are shown in black; meanders are shown in red. The black line shows a linear regression between the upper- and lower-layer velocity anomalies. (b) Scatterplot of the barotropic velocity against the upper (red) and lower (blue) layer velocity anomalies. The black line is a reference line with slope of 1.

since they impact the Atlantic meridional overturning circulation (AMOC) due to their comparatively warm and salty properties (Biastoch et al. 2008; Beal et al. 2011). Previous observational estimates of Agulhas leakage heat flux have focused on Eulerian observations of waters entrapped within Agulhas rings. These estimates are spread over an order of magnitude, from 0.023 PW (Gordon 1985) to 0.34 PW (McDonagh et al. 1999), and they omit leakage waters found outside Agulhas rings.

Here we estimate Agulhas leakage heat flux by combining our ASCA volume and temperature transports with a new Lagrangian estimate of leakage volume flux. Daher et al. (2020) observed that 27.9% of floats and drifters leak into the Atlantic, giving an estimated volume flux of 21 ± 5 Sv. This new estimate is 6 Sv larger than the previous seminal estimate by Richardson (2007), owing to additional leakage below 1000 m that was previously unaccounted for. To make our estimate of Agulhas leakage heat flux we assume that water mass properties are conserved between the location of the ASCA array and the South Atlantic and that leakage below 2000 m is negligible. We take the mean Benguela Current temperature profile from Garzoli and Gordon (1996) as representative of South Atlantic background properties.

Our climatological Agulhas leakage heat flux is then calculated by multiplying the constant ρC_p by the difference in time-mean upper-2000-m Agulhas Current temperature minus upper-2000-m Benguela Current temperature, times the time-mean volume transport multiplied by the 27.9% of water that leaks. This yields a heat flux of 0.2 PW, similar to that estimated by an ocean model study (Biastoch et al. 2015) and toward the higher end of previous observational estimates. The heat transport of the Atlantic Ocean at 32°S is estimated to be 0.62 ± 0.15 PW (Lumpkin and Speer 2007). Therefore, our estimate suggests that Agulhas leakage contributes about one-third of the northward heat transport of the South Atlantic.

5. Conclusions

The mean temperature transport of the Agulhas Current jet is 3.8 ± 0.2 PW southward, relative to 0°C. This is more than 1 PW larger than the temperature transport of the Florida Current or Kuroshio (Molinari et al. 1990; Zhang et al. 2002), although those measurements were conducted at latitudes equatorward of the ASCA array. The Agulhas Current dominates the heat budget of the Indian Ocean basin, with a temperature transport 3.5 times the 3-yr time-mean temperature transport of the Indonesian Throughflow (1.08 PW; Sprintall et al. 2009). The Agulhas Current also contributes about one-third of the northward heat transport of the South Atlantic through Agulhas leakage, confirming its influence beyond the Indian Ocean.

The temperature transport of the Agulhas Current is highly variable, with a standard deviation that is one-quarter of the time-mean value. This is due to high variability in both volume transport and transport-weighted temperature. Hence, using volume transport as a proxy for temperature transport by assuming a constant transport-weighted temperature results in a significant error of 0.24 PW. The southern Indian Ocean heat transport is estimated to be 1–1.5 PW southward (Hernández-Guerra and Talley 2016; Macdonald 1998; Ganachaud et al. 2000; Lumpkin and Speer 2007), and so the 0.24-PW error induced by assuming a constant Agulhas Current temperature may be one quarter of the basinwide heat transport. Therefore, measurements of both volume transport and temperature of the Agulhas Current are necessary to resolve variability in southern Indian Ocean heat transport.

The transport-weighted temperature of the Agulhas Current is related to its volume transport, albeit nonlinearly. This is different from the Florida Current, where no relationship is observed between the transport-weighted temperature and the volume transport (Shoosmith et al. 2005). This difference may be caused by the different bathymetry under each current. The Florida Current is shallower and more confined due to the boundaries on each side of the current, which limits deepening

or broadening. In contrast, the Agulhas Current can broaden to the east and deepen to almost 4500 m. During periods of strong southward temperature transport, the extent of southward flow is deeper and broader than during periods of weak southward temperature transport (Fig. 7). This is linked to a steepening of isotherms across the current and an increase in southward velocities that is consistent with geostrophy and with a dominant surface mode (Figs. 10b,d, 7d). The deepening and broadening of the current explain 52% of the variance in the temperature transport and may play an important role in southern Indian Ocean meridional heat transport.

The primary mode of Agulhas Current temperature field variability is caused by offshore meanders of the current (Fig. 10a). Meanders cool the transport-weighted temperature of the current by 1°C, without causing a significant change in the streamwise volume transport (Leber and Beal 2014). This suggests that an Agulhas Current with increased meandering due to increased eddy activity (Beal and Elipot 2016) may transport less heat, even while volume transport is unchanged, which could impact the southern Indian Ocean meridional heat transport. In addition, the deepening and broadening mode, which is the primary mode of temperature transport variability of the Agulhas Current, may impact the basinwide meridional heat transport. We plan to investigate basinwide meridional heat transport in a future paper by combining the ASCA data with Argo and satellite data across the interior of the southern Indian Ocean.

Acknowledgments. This work was funded by National Science Foundation Award 1459543. We thank Bradley Blows and Nauti-Buoys for building the ASCA moorings and leading deck operations on deployment and recovery, the Royal Netherlands Institute for Sea Research for their instrumentation contributions, and the crews of the RS *Algoa* and SA *Agulhas*.

Data availability statement. Individual instrument records (current meters, microCATs, and CPIES) collected during ASCA are available online (accession.nodc.noaa.gov/0209237 and accession.nodc.noaa.gov/0210643), as are gridded temperature, salinity, and velocity fields (beal-agulhas.rsmas.miami.edu/data-and-products). Hydrographic data were obtained from the NOAA National Centers for Environmental Information (https://www.ngdc.noaa.gov/ngdc.html). Argo data were obtained from U.S. GDAC (ftp://usgodae.org/pub/outgoing/argo). These data were collected and made freely available by the international Argo project and the national programs that contribute to it (https://doi.org/10.17882/42182). Previous hydrographic data were obtained from the National Centers for Environmental Information (https://www.ncei.noaa.gov/). The GMPE SST product is available through Copernicus Marine Environmental Monitoring Service (http://marine.copernicus.eu/services-portfolio/access-to-products/?option=com_csw&view=details&product_id=SST_GLO_SST_L4_NRT_OBSERVATIONS_010_005). The along-track sea level anomaly is publicly available through Copernicus Marine Environmental Monitoring Service (http://marine.copernicus.eu/services-portfolio/access-to-products/?option=com_csw&view=details&product_id=SEALEVEL_GLO_PHY_L3_REP_OBSERVATIONS_008_062). The BEST data are available online (https://cchdo.ucsd.edu/cruise/74DI202).

REFERENCES

Andres, M., V. Mensah, M. Chang, Y. Yang, C. M. Lee, B. Ma, and T. Sanford, 2017: Downstream evolution of the Kuroshio's time-varying transport and velocity structure. *J. Geophys. Res. Oceans*, **122**, 3519–3542, https://doi.org/10.1002/2016JC012519.

Beal, L. M., and H. L. Bryden, 1999: The velocity and vorticity structure of the Agulhas Current at 32°S. *J. Geophys. Res.*, **104**, 5151–5176, https://doi.org/10.1029/1998JC900056.

——, and S. Elipot, 2016: Broadening not strengthening of the Agulhas Current since the early 1990s. *Nature*, **540**, 570–573, https://doi.org/10.1038/NATURE19853.

——, T. K. Chereskin, Y. D. Lenn, and S. Elipot, 2006: The sources and mixing characteristics of the Agulhas Current. *J. Phys. Oceanogr.*, **36**, 2060–2074, https://doi.org/10.1175/JPO2964.1.

——, and Coauthors, 2011: On the role of the Agulhas system in ocean circulation and climate. *Nature*, **472**, 429–436, https://doi.org/10.1038/nature09983.

——, S. Elipot, A. Houk, and G. M. Leber, 2015: Capturing the transport variability of a western boundary jet: Results from the Agulhas Current Time-Series Experiment (ACT). *J. Phys. Oceanogr.*, **45**, 1302–1324, https://doi.org/10.1175/JPO-D-14-0119.1.

Biastoch, A., C. W. Böning, and J. R. Lutjeharms, 2008: Agulhas leakage dynamics affects decadal variability in Atlantic overturning circulation. *Nature*, **456**, 489–492, https://doi.org/10.1038/nature07426.

——, J. V. Durgadoo, A. K. Morrison, E. van Sebille, W. Weijer, and S. M. Griffies, 2015: Atlantic multi-decadal oscillation covaries with Agulhas leakage. *Nat. Commun.*, **6**, 10082, https://doi.org/10.1038/ncomms10082.

Brink, K. H., and J. Pedlosky, 2020: The structure of baroclinic modes in the presence of baroclinic mean flow. *J. Phys. Oceanogr.*, **50**, 239–253, http://doi.org/10.1175/JPO-D-19-0123.1.

Bryden, H. L., and L. M. Beal, 2001: Role of the Agulhas Current in Indian Ocean circulation and associated heat and freshwater fluxes. *Deep-Sea Res. I*, **48**, 1821–1845, https://doi.org/10.1016/S0967-0637(00)00111-4.

Daher, H., L. M. Beal, and F. U. Schwarzkopf, 2020: A new improved estimation of Agulhas leakage using observations and simulations of Lagrangian floats and drifters. *J. Geophys. Res. Oceans*, **125**, e2019JC015753, https://doi.org/10.1029/2019JC015753.

Donohue, K. A., D. R. Watts, K. L. Tracey, A. D. Greene, and M. Kennelly, 2010: Mapping circulation in the Kuroshio extension with an array of current and pressure recording inverted echo sounders. *J. Atmos. Oceanic Technol.*, **27**, 507–527, https://doi.org/10.1175/2009JTECHO686.1.

Elipot, S., and L. M. Beal, 2015: Characteristics, energetics, and origins of Agulhas current meanders and their limited influence on ring shedding. *J. Phys. Oceanogr.*, **45**, 2294–2314, https://doi.org/10.1175/JPO-D-14-0254.1.

——, and ——, 2018: Observed Agulhas current sensitivity to interannual and long-term trend atmospheric forcings. *J. Climate*, **31**, 3077–3098, http://doi.org/10.1175/JCLI-D-17-0597.1.

Fillenbaum, E. R., T. N. Lee, W. E. Johns, and R. Zantopp, 1997: Meridional heat transport variability at 26.5°N in the North Atlantic. *J. Phys. Oceanogr.*, **27**, 153–174, https://doi.org/10.1175/1520-0485(1997)027<0153:MHTVAN>2.0.CO;2.

Ganachaud, A., C. Wunsch, J. Marotzke, and J. Toole, 2000: Meridional overturning and large-scale circulation of the Indian Ocean. *J. Geophys. Res.*, **105**, 26 117–26 134, https://doi.org/10.1029/2000JC900122.

Garzoli, S. L., and A. L. Gordon, 1996: Origins and variability of the Benguela current. *J. Geophys. Res.*, **101**, 897–906, https://doi.org/10.1029/95JC03221.

Gordon, A. L., 1985: Indian-Atlantic transfer of thermocline water at the Agulhas retroflection. *Science*, **227**, 1030–1033, https://doi.org/10.1126/science.227.4690.1030.

Goschen, W. S., T. G. Bornman, S. H. P. Deyzel, and E. H. Schumann, 2015: Coastal upwelling on the far eastern Agulhas Bank associated with large meanders in the Agulhas Current. *Cont. Shelf Res.*, **101**, 34–46, https://doi.org/10.1016/j.csr.2015.04.004.

Gunn, K. L., L. M. Beal, S. Elipot, K. McMonigal, and A. Houk, 2020: Mixing of subtropical, central, and intermediate waters driven by shifting and pulsing of the Agulhas Current. *J. Phys. Oceanogr.*, **50**, 3545–3560, https://doi.org/10.1175/JPO-D-20-0093.1.

Hall, M. M., and H. L. Bryden, 1982: Direct estimates and mechanisms of ocean heat transport. *Deep-Sea Res.*, **29**, 339–359, https://doi.org/10.1016/0198-0149(82)90099-1.

Hernández-Guerra, A., and L. D. Talley, 2016: Meridional overturning transports at 30°S in the Indian and Pacific Oceans in 2002–2003 and 2009. *Prog. Oceanogr.*, **146**, 89–120, https://doi.org/10.1016/J.POCEAN.2016.06.005.

Hutchinson, K., L. M. Beal, P. Penven, I. Ansorge, and J. Hermes, 2018: Seasonal phasing of Agulhas current transport tied to a baroclinic adjustment of near-field winds. *J. Geophys. Res. Oceans*, **123**, 7067–7083, https://doi.org/10.1029/2018JC014319.

Johns, W. E., T. Kanzow, and R. Zantopp, 2005: Estimating ocean transports with dynamic height moorings: An application in the Atlantic Deep Western Boundary Current at 26°N. *Deep-Sea Res. I*, **52**, 1542–1567, https://doi.org/10.1016/j.dsr.2005.02.002.

Joyce, T. M., 1988: The WOCE hydrographic program. *Eos, Trans. Amer. Geophys. Union*, **69**, 68–70, https://doi.org/10.1029/88EO00050.

Kanzow, T., U. Send, W. Zenk, A. D. Chave, and M. Rhein, 2006: Monitoring the integrated deep meridional flow in the tropical North Atlantic: Long-term performance of a geostrophic array. *Deep-Sea Res. I*, **53**, 528–546, https://doi.org/10.1016/j.dsr.2005.12.007.

——, and Coauthors, 2010: Seasonal variability of the Atlantic meridional overturning circulation at 26.5°N. *J. Climate*, **23**, 5678–5698, https://doi.org/10.1175/2010JCLI3389.1.

Kersalé, M., and Coauthors, 2019: Shallow and deep eastern boundary currents in the South Atlantic at 34.5°S: Mean structure and variability. *J. Geophys. Res. Oceans*, **124**, 1634–1659, https://doi.org/10.1029/2018JC014554.

LaCasce, J. H., 2017: The prevalence of oceanic surface modes. *Geophys. Res. Lett.*, **44**, 11 097–11 105, https://doi.org/10.1002/2017GL075430.

Leber, G. M., and L. M. Beal, 2014: Evidence that Agulhas current transport is maintained during a meander. *J. Geophys. Res.*, **119**, 3806–3817, https://doi.org/10.1002/2014JC009802.

——, ——, and S. Elipot, 2017: Wind and current forcing combine to drive strong upwelling in the Agulhas current. *J. Phys. Oceanogr.*, **47**, 123–134, https://doi.org/10.1175/JPO-D-16-0079.1.

Lumpkin, R., and K. Speer, 2007: Global ocean meridional overturning. *J. Phys. Oceanogr.*, **37**, 2550–2562, https://doi.org/10.1175/JPO3130.1.

Macdonald, A. M., 1998: The global ocean circulation: A hydrographic estimate and regional analysis. *Prog. Oceanogr.*, **41**, 281–382, https://doi.org/10.1016/S0079-6611(98)00020-2.

Martin, M., and Coauthors, 2012: Group for High Resolution Sea Surface temperature (GHRSST) analysis fields inter-comparisons. Part I: A GHRSST multi-product ensemble (GMPE). *Deep-Sea Res. II*, **77-80**, 21–30, https://doi.org/10.1016/j.dsr2.2012.04.013.

McDonagh, E. L., K. J. Heywood, and M. P. Meredith, 1999: On the structure, paths, and fluxes associate with Agulhas rings. *J. Geophys. Res.*, **104**, 21 007–21 020, https://doi.org/10.1029/1998JC900131.

——, and Coauthors, 2015: Continuous estimate of Atlantic oceanic freshwater flux at 26.5°N. *J. Climate*, **28**, 8888–8906, https://doi.org/10.1175/JCLI-D-14-00519.1.

McDougall, T. J., and P. Barker, 2011: Getting started with TEOS-10 and the Gibbs Seawater (GSW) oceanographic toolbox. Scientific Committee on Oceanic Research/International Association for the Physical Sciences of the Oceans Tech. Rep. SCOR/IAPSO WG127, 28 pp., http://www.teos-10.org/pubs/Getting_Started.pdf.

Meinen, C. S., and D. R. Watts, 2000: Vertical structure and transport on a transect across the North Atlantic Current near 42°N: Time series and mean. *J. Geophys. Res.*, **105**, 21 869–21 891, https://doi.org/10.1029/2000JC900097.

Mohino, E., S. Janicot, and J. Bader, 2011: Sahel rainfall and decadal to multi-decadal sea surface temperature variability. *Climate Dyn.*, **37**, 419–440, https://doi.org/10.1007/s00382-010-0867-2.

Molinari, R. L., E. Johns, and J. F. Festa, 1990: The annual cycle of meridional heat flux in the Atlantic Ocean at 26.5°N. *J. Phys. Oceanogr.*, **20**, 476–482, https://doi.org/10.1175/1520-0485(1990)020<0476:TACOMH>2.0.CO;2.

Njouodo, A. S. N., S. Koseki, N. Keenlyside, and M. Rouault, 2018: Atmospheric signature of the Agulhas Current. *Geophys. Res. Lett.*, **45**, 5185–5193, https://doi.org/10.1029/2018GL077042.

Richardson, P. L., 2007: Agulhas leakage into the Atlantic estimated with subsurface floats and surface drifters. *Deep-Sea Res. I*, **54**, 1361–1389, https://doi.org/10.1016/j.dsr.2007.04.010.

Rouault, M., 2002: Ocean–atmosphere interaction in the Agulhas Current region and a South African extreme weather event. *Wea. Forecasting*, **17**, 655–669, https://doi.org/10.1175/1520-0434(2002)017<0655:OAIITA>2.0.CO;2.

Rouault, M. J., and P. Penven, 2011: New perspectives on Natal Pulses from satellite observations. *J. Geophys. Res.*, **116**, L23603, https://doi.org/10.1029/2010JC006866.

Roullet, G., X. Capet, and G. Maze, 2014: Global interior eddy available potential energy diagnosed from Argo floats. *Geophys. Res. Lett.*, **41**, 1651–1656, https://doi.org/10.1002/2013GL059004.

Shoosmith, D. R., M. O. Baringer, and W. E. Johns, 2005: A continuous record of Florida Current temperature transport at 27°N. *Geophys. Res. Lett.*, **32**, L23603, https://doi.org/10.1029/2005GL024075.

Sprintall, J., S. E. Wijffels, R. Molcard, and I. Jaya, 2009: Direct estimates of the Indonesian throughflow entering the Indian Ocean: 2004–2006. *J. Geophys. Res.*, **114**, 2004–2006, https://doi.org/10.1029/2008JC005257.

Tsugawa, M., and H. Hasumi, 2010: Generation and growth mechanism of the natal pulse. *J. Phys. Oceanogr.*, **40**, 1597–1612, https://doi.org/10.1175/2010JPO4347.1.

Zhang, D., W. E. Johns, and T. N. Lee, 2002: The seasonal cycle of meridional heat transport at 24°N in the north Pacific and in the global ocean. *J. Geophys. Res.*, **107**, 3083, https://doi.org/10.1029/2001JC001011.